Green Chemistry

PAPER

View Article Online
View Journal | View Issue

Cite this: *Green Chem.*, 2025, **27**, 14547

Combined catalyst–pathway design for efficient and green urea synthesis

Zhuohang Li, Xuezi Xing, Ruichao Zhang, Xue Zeng * and Ke Chu *

Received 2nd September 2025,
Accepted 22nd October 2025

DOI: 10.1039/d5gc04601g

rsc.li/greenchem

Urea electrosynthesis from CO_2 + NO_3^- co-electrolysis (UECN) offers a promising pathway for sustainable urea synthesis, while necessitating rational catalyst/pathway design to boost CO_2/NO_3^- co-activation and C–N coupling. Herein, we demonstrate an atomically dispersed Ag on oxygen vacancy (OV)-rich TiO_2 (Ag_1/TiO_{2-x}) catalyst for efficient UECN. Theoretical calculations and *in situ* spectroscopic analyses reveal the synergy of OV-induced $Ag_{1\text{-}OV}$ and Ti_{OV} dual-sites in promoting the selective C–N coupling of *CO and $*NO_2$ for target urea generation. Notably, with the integration of plasma-assisted air-to-NO_x^- conversion and CO_2 + NO_x^- co-electrolysis, Ag_1/TiO_{2-x} achieves an exceptional urea faradaic efficiency of 75.7% and a urea yield rate of 74.6 mmol h^{-1} g^{-1} along with excellent catalytic stability.

Green foundation

1. We pioneer a plasma-electrocatalytic pathway for efficient and green urea synthesis using atmospheric air (N_2/O_2) and CO_2 as feedstocks, eliminating fossil fuel-derived NH_3 required in conventional processes. The Ag_1/TiO_{2-x} catalyst enables selective C–N coupling of *CO/$*NO_2$ intermediates *via* dual-site synergy for target urea generation.
2. Quantitatively, our strategy achieves a record-high urea faradaic efficiency of 75.7% and urea yield rate of 74.6 mmol h^{-1} g^{-1} along with excellent catalytic stability. Qualitatively, it bypasses the energy-intensive Haber–Bosch process and enables much lower energy consumption *versus* industrial urea synthesis under mild conditions.
3. Future work should optimize plasma energy efficiency using renewable electricity and scale catalyst loading and membrane-electrode assemblies for industrial deployment.

Urea ($CO(NH_2)_2$) plays a vital role in agricultural and industrial development.[1] The industrial urea synthesis remains tethered to the energy-intensive Bosch–Meiser process under harsh conditions, giving rise to enormous global energy consumption and huge CO_2 emissions.[2] Electrocatalytic C–N coupling of CO_2 and nitrogenous species (*i.e.*, N_2/NO_3^-) offers a promising alternative pathway for sustainable urea synthesis by repurposing waste carbon/nitrogen sources while leveraging renewable energy.[3–6] Recent studies have demonstrated the feasibility of urea electrosynthesis from CO_2 + NO_3^- co-electrolysis (UECN), simultaneously realizing environmental remediation and value-added urea production.[7] Nevertheless, UECN faces sluggish reaction kinetics due to the inefficient C–N coupling and low selectivity from competing reaction pathways (NO_3^--to-NH_3 reduction reaction (NO_3RR) and hydrogen evolution reaction (HER)).[8–11] These challenges necessitate innovative UECN catalyst/pathway design to enhance activity, selectivity and stability for efficient and durable urea electrosynthesis.

Recent advances highlight single-atom catalysts (SACs) and oxygen vacancy (OV) engineering as promising strategies, in which SACs maximize atom utilization and tailor active sites, while OVs modulate the catalyst electronic structure to enhance intermediate stabilization and accelerate charge transfer.[12–14] For instance, integrating metal single atoms into OV-rich oxides can effectively boost CO_2 activation and concurrently leverage metal–support interactions to promote C–N coupling.[14–18] Despite these merits, simultaneously achieving high urea yield rate and faradaic efficiency (FE_{urea}) remains challenging due to the competitive adsorption of various C/N reactants, inherent scaling relations in multi-step reactions, and insufficient stabilization of key C/N intermediates.[10] In addition, the NO_3^- feedstocks still indirectly depend on fossil fuels, which undermines the process sustainability, thus underscoring the need for nitrogen sources that require facile activation with sustainable production.[19]

Herein, we demonstrate an atomically dispersed Ag on OV-rich TiO_2 (Ag_1/TiO_{2-x}) catalyst for efficient UECN. By combining extensive experimental and theoretical calculations, we elu-

School of Materials Science and Engineering, Lanzhou Jiaotong University, Lanzhou 730070, China. E-mail: zengxue@lzjtu.edu.cn, chuk630@mail.lzjtu.cn

cidate how Ag single atoms and OV-rich TiO_{2-x} synergistically promote C–N coupling while suppressing the competing side reactions towards efficient and selective urea generation. Notably, with integration of plasma-assisted air-to-NO_x^- conversion and CO_2 + NO_x^- co-electrolysis, Ag_1/TiO_{2-x} exhibits outstanding UECN performance, achieving an FE_{urea} of 75.7% and a urea yield rate of 74.6 mmol h^{-1} g^{-1} along with excellent catalytic stability.

Ag_1/TiO_{2-x} was synthesized through a combined hydrothermal/annealing method. The XRD pattern (Fig. S1) of Ag_1/TiO_{2-x} reveals the characteristic TiO_2 diffraction peaks (PDF#86-1157) with no Ag-related species observed, indicating that the introduced Ag species are ultrasmall and highly dispersed on TiO_{2-x}. A typical nanosheet morphology is observed in the TEM images of Ag_1/TiO_{2-x} (Fig. 1a and Fig. S2a). The HRTEM (Fig. S2b) image of Ag_1/TiO_{2-x} displays clear lattice fringes with an interplanar distance of 0.352 nm, assigned to the (101) plane of Ag_1/TiO_{2-x}. The AC-STEM (Fig. 1b) image of Ag_1/TiO_{2-x} displays numerous atomically dispersed bright spots, assigned to isolated Ag atoms. The atomic-level isolation of Ag species can be further confirmed by the corresponding atomic intensity line scanning and 3D surface intensity profile (Fig. 1c). Elemental mapping images of Ag_1/TiO_{2-x} (Fig. 1d) reveal a homogeneous dispersion of Ag atoms on the TiO_{2-x} substrate. Inductively coupled plasma analysis shows that the Ag content is 3.37 wt%. The EPR spectra (Fig. S3) display much stronger g-signals of TiO_{2-x} and Ag_1/TiO_{2-x} relative to bulk TiO_2, indicating the existence of rich oxygen vacancies (OVs) on both TiO_{2-x} and Ag_1/TiO_{2-x}. Meanwhile, Ag_1/TiO_{2-x} exhibits a similar g-signal intensity to TiO_{2-x}, implying that the introduced Ag species have little impact on the OV concentration of TiO_{2-x}.

XAS is used to study the coordination and valence environment of Ag_1/TiO_{2-x}. The XANES (Fig. 1e) spectra reveal that the Ag K-edge of Ag_1/TiO_{2-x} is located between Ag foil (0) and Ag_2O (+1), and linear fitting analysis reveals an average Ag valence state of +0.65 for Ag_1/TiO_{2-x} (Fig. S4). The EXAFS spectra (Fig. 1f) of Ag_1/TiO_{2-x} exhibit prominent Ag–O coordination with no Ag–Ag coordination (2.75 Å) observed, suggesting that the loaded Ag species are atomically dispersed

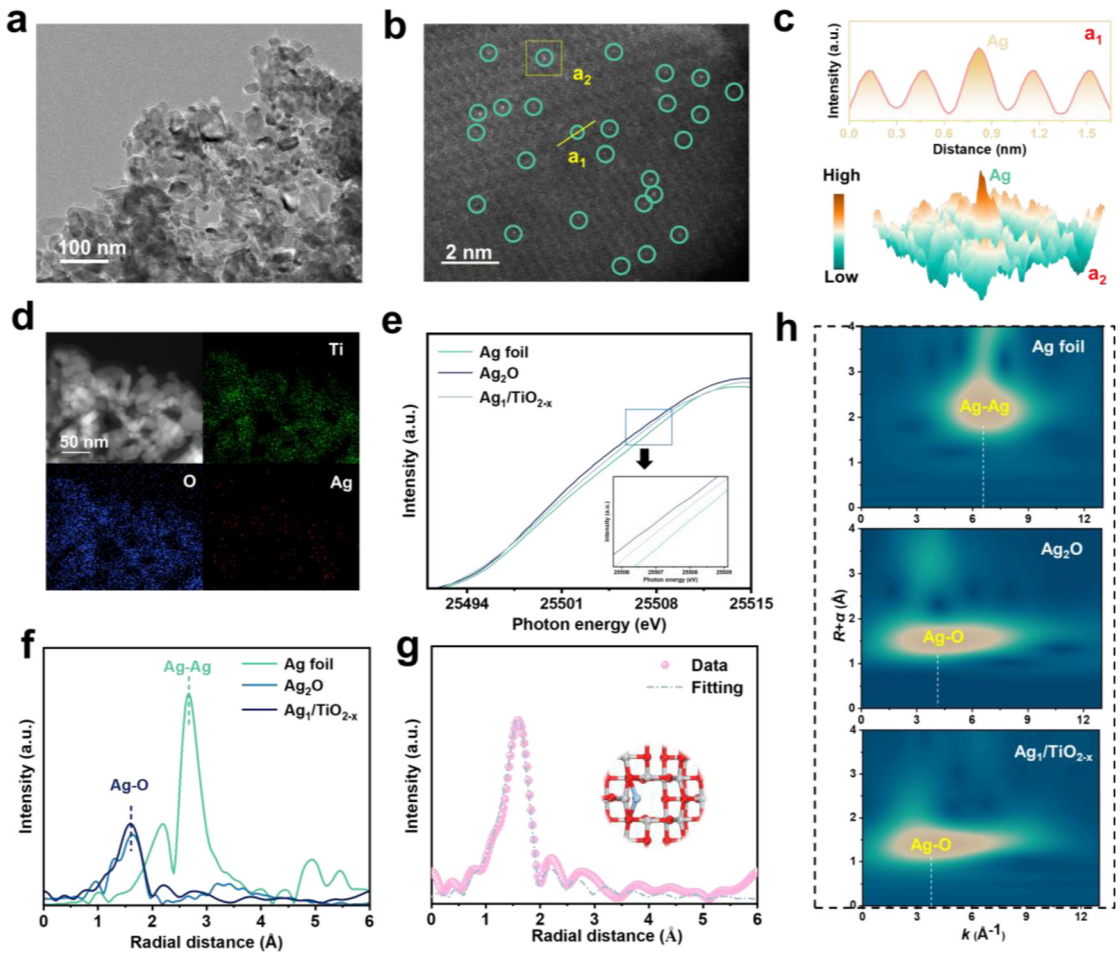

Fig. 1 (a–d) Characterization of Ag_1/TiO_{2-x}: (a) TEM image, (b) AC-STEM image and the corresponding (c) intensity line scanning profile and 3D intensity profile, and (d) elemental mapping images. (e–h) Ag K-edge XAS analyses: (e) XANES spectra, (f) EXAFS spectra, (g) EXAFS fitting curve of Ag_1/TiO_{2-x} and (h) wavelet transform analyses of Ag foil, Ag_2O and Ag_1/TiO_{2-x}.

on the TiO_{2-x} substrate,[20–22] thus ruling out the formation of Ag nanoparticles or clusters. Quantitative EXAFS fitting analysis (Fig. 1g) shows that the isolated Ag atoms are coordinated with two surrounding O atoms, forming an Ag–O_2 geometric unit (Fig. 1g, inset, Table S1). The corresponding wavelet transform contour plots (Fig. 1h) reveal a sole intensity maximum of Ag–O at 3.9 $Å^{-1}$ for Ag_1/TiO_{2-x}, further confirming that isolated Ag atoms are highly dispersed on the TiO_{2-x} substrate.

DFT calculations were carried out to elucidate the electronic structure of Ag_1/TiO_{2-x} (Fig. S5). Differential charge density maps (Fig. S6) show more enriched electron density of Ag_1/TiO_{2-x} compared to TiO_2, TiO_{2-x} and Ag_1/TiO_2, suggesting that OV and Ag_1 are both favorable for boosting the electronic interaction and this is further verified by the remarkable Ag/O/Ti orbital hybridization shown by the partial density of states (PDOS, Fig. S7). In addition, Ag_1/TiO_{2-x} reveals the equilibrium energy and temperature states below 698 K (Fig. S8) during the simulation, verifying the excellent thermodynamic stability of Ag_1/TiO_{2-x}. Furthermore, the Ag_1 introduction modulates the electronic structure of TiO_{2-x} to cause a decreased work function of Ag_1/TiO_{2-x} (Fig. S9), thereby facilitating efficient proton-coupled electron transfer to promote the electrocatalytic UECN kinetics.[23–25]

The electrochemical UECN performance of Ag_1/TiO_{2-x} was first evaluated in an H-cell containing a CO_2-saturated electrolyte (0.1 M KNO_3 and 0.1 M $KHCO_3$).[26] Liquid and gas products were detected using colorimetric and gas chromatographic methods (Fig. S10), respectively. Linear sweep voltammetry (LSV, Fig. S11a) curves show that compared to the Ar-saturated electrolyte, the CO_2-saturated electrolyte presents a relatively higher current density (j), suggesting the pronounced catalytic UECN activity of Ag_1/TiO_{2-x}. A chronoamperometric test for 1 h of electrolysis at various potentials (Fig. S11b) was then performed to quantitatively determine the produced urea on Ag_1/TiO_{2-x}. As shown in Fig. 2a, Ag_1/TiO_{2-x} exhibits the highest FE_{urea} of 40.1% with a corresponding urea yield rate of 25.9 mmol h^{-1} g^{-1} at −0.7 V, which are higher than those of most reported catalysts (Table S2). The FEs of other by-products were also tested with NH_3 being the primary by-product (Fig. 2b).

Several tests were carried out to verify the N/C sources of the produced urea. ^1H nuclear magnetic resonance (NMR)

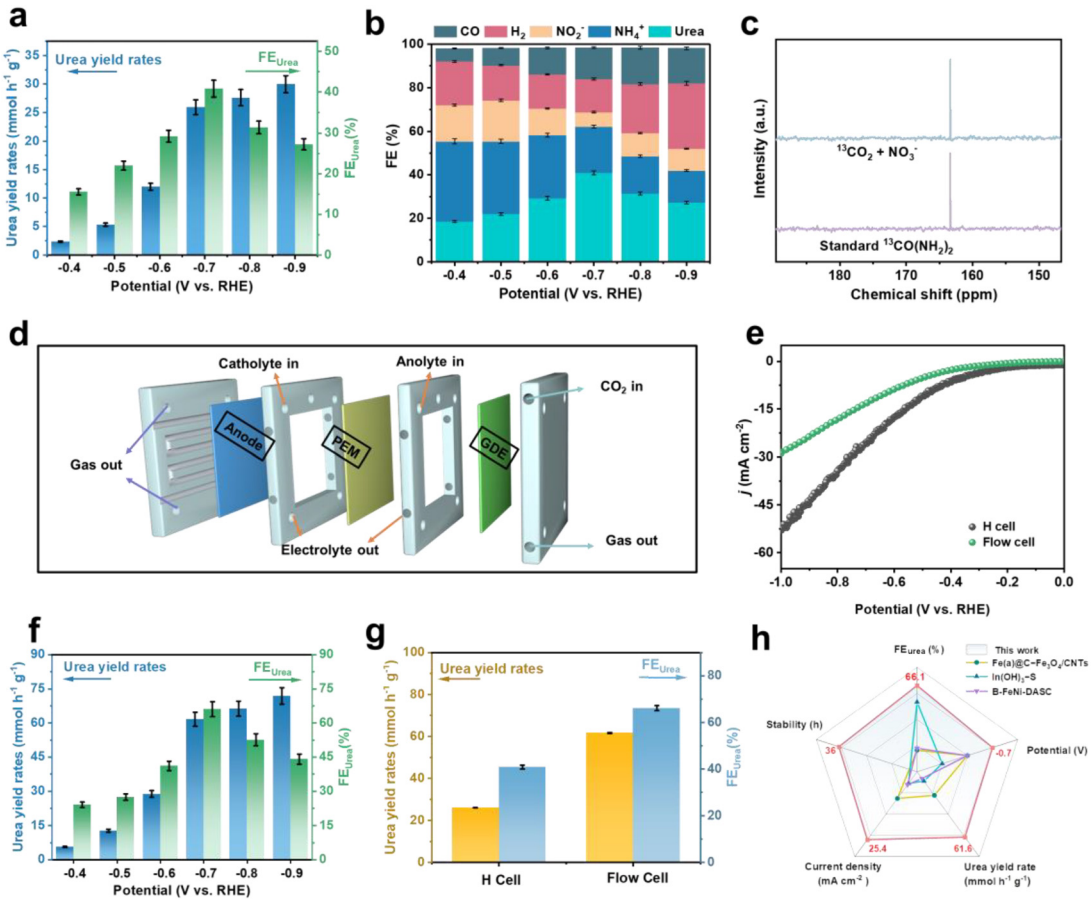

Fig. 2 (a) UECN performances of Ag_1/TiO_{2-x} at different potentials. (b) FEs of different products on Ag_1/TiO_{2-x}. (c) ^{13}C NMR spectra of the $^{13}CO(NH_2)_2$ standard sample and those fed with $^{13}CO_2$ after electrolysis at −0.7 V. (d) Schematic diagram of the flow cell. (e) LSV curves of Ag_1/TiO_{2-x} in an H-cell and flow cell. (f) UECN performances of Ag_1/TiO_{2-x} at different potentials in the flow cell. (g) Comparison of urea yield rates and FE_{urea} in the H-cell and flow cell. (h) Comparison of the catalytic performance between Ag_1/TiO_{2-x} and recently reported catalysts.

experiments show that using $^{15}NO_3^-$ as the N-source results in a characteristic doublet chemical shift of CO $(^{15}NH_2)_2$ (Fig. S12), while employing $^{13}CO_2$ leads to a typical singlet chemical shift of $^{13}CO(NH_2)_2$ (Fig. 2c), evidencing that urea is exclusively produced through combined CO_2 and NO_x^-. Fig. S13 shows negligible urea detection without the CO_2 feeding gas, in an NO_x^--free electrolyte or at the open circuit potential (OCP), suggesting that the generated urea originates from the UECN process. We further studied the long-term electrolysis of Ag_1/TiO_{2-x}, which showed a rather stable current density (Fig. S14), indicating the good long-term stability of Ag_1/TiO_{2-x}. In addition, as shown in Fig. S15 during the eight consecutive electrolysis cycles, FE_{urea} and urea yield rate show no obvious changes, indicating the outstanding cycling stability of Ag_1/TiO_{2-x}.[27–29] After the stability test, Ag_1/TiO_{2-x} retains the atomic Ag dispersion and Ag content (Fig. S16), confirming the robust structure of Ag_1/TiO_{2-x}.[30,31]

Generally, the low CO_2 solubility and mass transfer limitation of an H-cell give rise to compromised UECN performance. To further improve the UECN activity of Ag_1/TiO_{2-x}, we employed a flow cell (Fig. 2d) that can enhance the CO_2 mass transfer during UECN electrolysis. As shown in the LSV curves (Fig. 2e), Ag_1/TiO_{2-x} exhibits a much larger current density in the flow cell than in the H-cell, suggesting that the enhanced UECN activity of Ag_1/TiO_{2-x} is enabled by the flow cell. Quantitative measurement at various potentials (Fig. 2f and Fig. S17) shows that Ag_1/TiO_{2-x} in the flow cell reaches the maximum FE_{urea} of 66.1% with the corresponding urea yield rate of 61.6 mmol h^{-1} g^{-1}, significantly outperforming its H-cell counterpart (Fig. 2g) and most reported catalysts (Fig. 2h and Fig. S18). Moreover, the current density remains virtually constant during 36 h of continuous electrolysis (Fig. S19) and there are no significant changes in the UECN performances for eight consecutive electrolysis cycles (Fig. S20),[32,33] highlighting the excellent UECN performance of the Ag_1/TiO_{2-x}/flow cell toward efficient and durable urea electrosynthesis.

To elucidate the underlying reasons for the enhanced UECN performance of Ag_1/TiO_{2-x}, *operando* FTIR spectroscopy was first employed to detect the key intermediates generated during the UECN electrolysis at various potentials. As displayed in Fig. 3a and b, Ag_1/TiO_{2-x} exhibits a pronounced infrared band of $*NO_2$ at 1430 cm^{-1}.[34] The infrared bands probed at 2050 cm^{-1} and 1330 cm^{-1} are assigned to *CO and *COOH, respectively.[35] The infrared band at 1400 cm^{-1} corresponds to the stretching mode of the C–N bond, while the bands at 1580 cm^{-1} and 1690 cm^{-1} are assigned to the generated $*CONO_2$ and $*CONH_2$ intermediates, respectively.[36,37] The pronounced bands of C–N bonds and $*CONO_2$ and $*CONH_2$ intermediates alongside the urea-related band (~1170 cm^{-1})[26] collectively confirm that Ag_1/TiO_{2-x} can effectively drive the UECN process and promote C–N coupling towards urea generation. Furthermore, online DEMS measurements (Fig. S21) show the distinct signals of $*CONO_2$ (m/z = 74), $*CONH_2$ (m/z = 44), $*NO_2$ (m/z = 46), *CO (m/z = 28) and *COOH (m/z = 45), while no signals of $*NO_2H$ (m/z = 47) can be found. The absence of the $*NO_2H$ intermediate and the presence of $*CONO_2$ and $*CONH_2$ intermediates disclose that Ag_1/TiO_{2-x} preferentially proceeds through the *CO + $*NO_2$ coupling pathway ($*NO_3 \rightarrow *NO_2 \rightarrow *CONO_2 \rightarrow$ *CONOOH $\rightarrow$ *CONO $\rightarrow$ *CONHO $\rightarrow$ *CONH $\rightarrow$ $*CONH_2 \rightarrow$ *CO $NO_2NH_2 \rightarrow$ urea) to drive the UECN process towards urea formation.

In stark contrast, pristine TiO_{2-x} (Fig. 3c) exhibits the dominant *CO band at 2050 cm^{-1} but negligible C–N (1400 cm^{-1}), $*CONO_2$ (1580 cm^{-1}) and $CONH_2$ (1690 cm^{-1}) signals, highlighting its limited C–N coupling capability despite efficient $CO_2 \rightarrow$ *CO conversion. This is further supported by the *operando* Raman spectra, where pristine TiO_{2-x} displays a weak N–C–N stretching band (Fig. 3e), in contrast to the much stronger N–C–N band observed in Ag_1/TiO_{2-x} (Fig. 3d). These *operando* FTIR/Raman results underscore the synergistic roles of Ag_1 and TiO_{2-x} in enhancing the UECN process, where TiO_{2-x} facilitates the reduction of CO_2 to *CO while Ag_1 promotes the conversion of NO_x^- to $*NO_2$ and drives the C–N coupling of generated $*NO_2$ and *CO for urea formation.

Theoretical computation was utilized to clarify the UECN mechanism of Ag_1/TiO_{2-x}. According to the previous XAS (Fig. 1e–h) and DFT results (Fig. S5–S7), four active sites on Ag_1/TiO_{2-x} are considered: the pristine Ti site, the Ag single-atom site (Ag_1), the OV-adjacent Ti site (Ti_{OV}), and the OV-adjacent Ag single-atom site ($Ag_{1\text{-}OV}$). Fig. 4a shows that among all four sites, NO_3^- is mostly preferentially adsorbed on the $Ag_{1\text{-}OV}$ site while $*CO_2$ is mostly preferentially adsorbed on the Ti_{OV} site. Accordingly, in the UECN process, the $Ag_{1\text{-}OV}$ site mainly drives NO_3^- reduction while the Ti_{OV} site drives $*CO_2$ reduction. The formed C-intermediates on the Ti_{OV} site and N-intermediates on the $Ag_{1\text{-}OV}$ site would undergo C–N coupling towards urea formation.

Previous *operando* FTIR results (Fig. 3a–c) indicate that $*NO_2$ is the critical N-intermediate in the UECN process. After analyzing the free energy barriers for the C–N coupling of $*NO_2$ with various C-intermediates (Fig. 4b and Fig. S22, S23), it is found that $*NO_2$ coupling with *CO shows the lowest energy barrier, suggesting that $*CO/*NO_2$ coupling is mostly energetically favored for urea formation. Likewise, for the C–N coupling of *CO with various N-intermediates, *CO coupling with $*NO_2$ shows the lowest energy barrier (Fig. 4c and Fig. S24). Thus, the UECN process on Ag_1/TiO_{2-x} involves two key steps, namely, the initial $CO_2 \rightarrow$ *CO and $*NO_3 \rightarrow *NO_2$ and the subsequent C–N coupling of $*NO_2$ and *CO to generate urea ($*NO_2$ + *CO $\rightarrow$ $*CONO_2 \rightarrow$ *CONOOH $\rightarrow$ *CONO $\rightarrow$ *CONHO $\rightarrow$ *CONH $\rightarrow$ $*CONH_2 \rightarrow$ *CO $NO_2NH_2 \rightarrow$ urea). For the $CO_2 \rightarrow$ *CO process, compared to the Ti site (0.73 eV), the Ti_{OV} site shows a much lower rate-determining step (RDS) energy barrier of 0.50 eV (Fig. 4d and Fig. S25–S27), indicating that Ti_{OV} serves as the primary site for $CO_2 \rightarrow$ *CO reduction, thus ensuring a steady supply of the *CO intermediate necessary for the subsequent C–N coupling with $*NO_2$ on the Ag_1 site. For the $NO_3^- \rightarrow *NO_2$ process (Fig. S28), the $Ag_{1\text{-}OV}$ site (0.55 eV) exhibits a larger downhill energy change than the Ag_1 site (0.83 eV), suggesting that the $Ag_{1\text{-}OV}$ site is more energetically effective in facilitating NO_3^- activation for $*NO_2$ for-

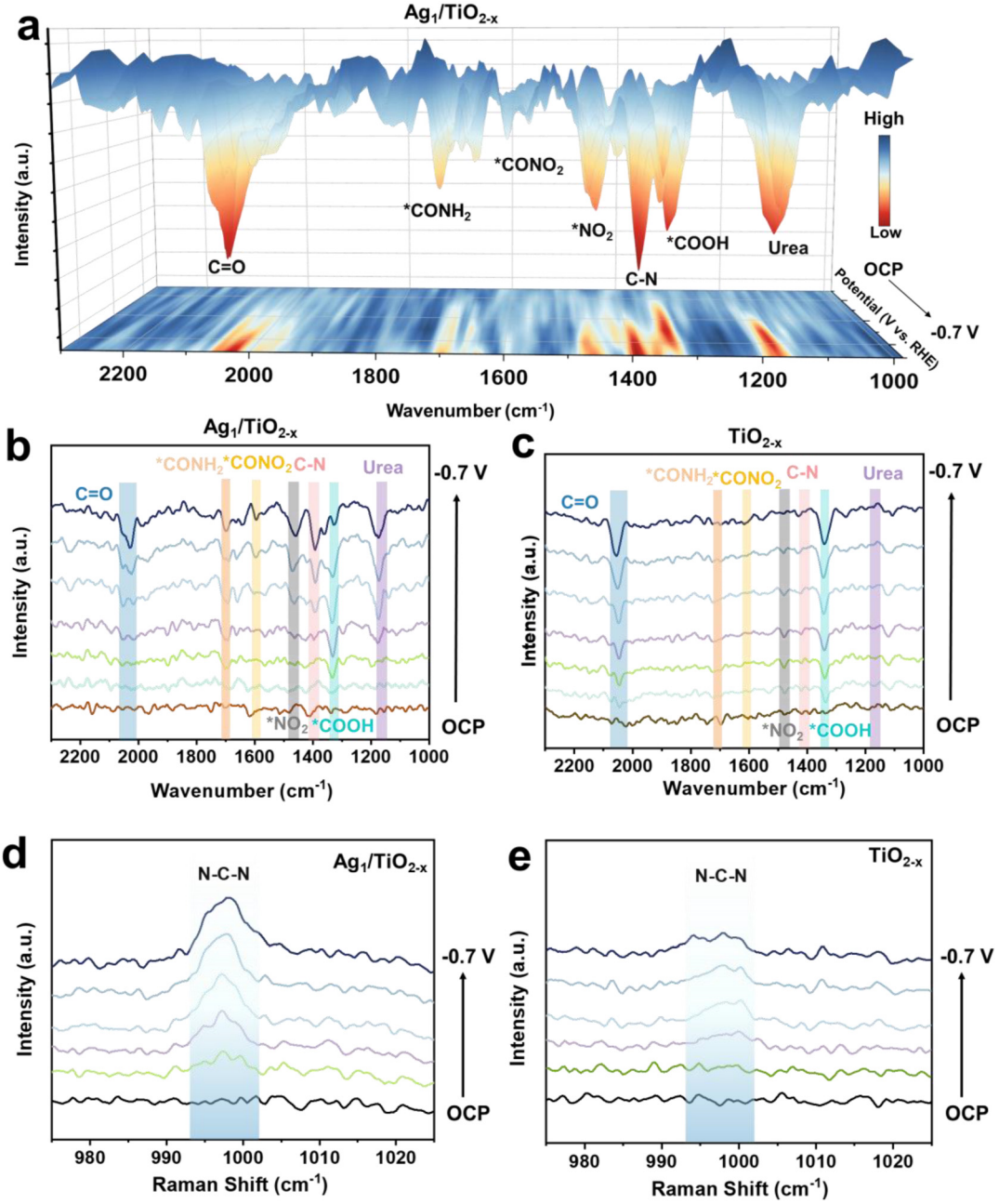

Fig. 3 *Operando* FTIR spectra of (a and b) Ag_1/TiO_{2-x} and (c) TiO_{2-x} during UECN electrolysis at various potentials. (d and e) *Operando* Raman spectra of (d) Ag_1/TiO_{2-x} and (e) TiO_{2-x} during UECN electrolysis at various potentials.

mation. These results demonstrate that OVs play a crucial role in enhancing the capabilities of both Ag_1 and Ti sites for CO_2/NO_2^- activation and reduction.

After the formation of *CO on the Ti_{OV} site and $*NO_2$ on the $Ag_{1\text{-}OV}$ site, we further investigated the electrocatalytic C–N coupling process required for urea synthesis. Before C–N coupling, *CO must migrate from Ti_{OV} to $Ag_{1\text{-}OV}$ or $*NO_2$ migration from $Ag_{1\text{-}OV}$ to Ti_{OV} must occur (Fig. S29 and S30). Transition state (TS) calculations reveal a lower energy barrier for *CO migration (0.63 eV, Fig. 4e) compared to $*NO_2$ migration (1.72 eV, Fig. 4f), indicating a kinetically favored *CO migration from Ti_{OV} to $Ag_{1\text{-}OV}$.[38,39] This preferential *CO migration facilitates effective C–N coupling with $*NO_2$ on the $Ag_{1\text{-}OV}$ site to form $*CONO_2$. After the migration of *CO from the Ti_{OV} site to the $Ag_{1\text{-}OV}$ site, the first C–N coupling of *CO and $*NO_2$ (*CO + $*NO_2$ → $*CONO_2$) and the second C–N coupling of $*CONH_2$ and $*NO_2$ ($*CONH_2$ + $*NO_2$ → $*CONH_2NO_2$) are energetically more favorable on the $Ag_{1\text{-}OV}$ site (0.37 eV and 0.21 eV) over the Ag_1 site (0.68 eV and 0.53 eV) (Fig. S31–S33). This indicates that C–N coupling for urea formation is more favorable on the $Ag_{1\text{-}OV}$ site. All these findings demonstrate the synergistic role of the $Ag_{1\text{-}OV}$ and Ti_{OV} sites in promoting urea synthesis, where

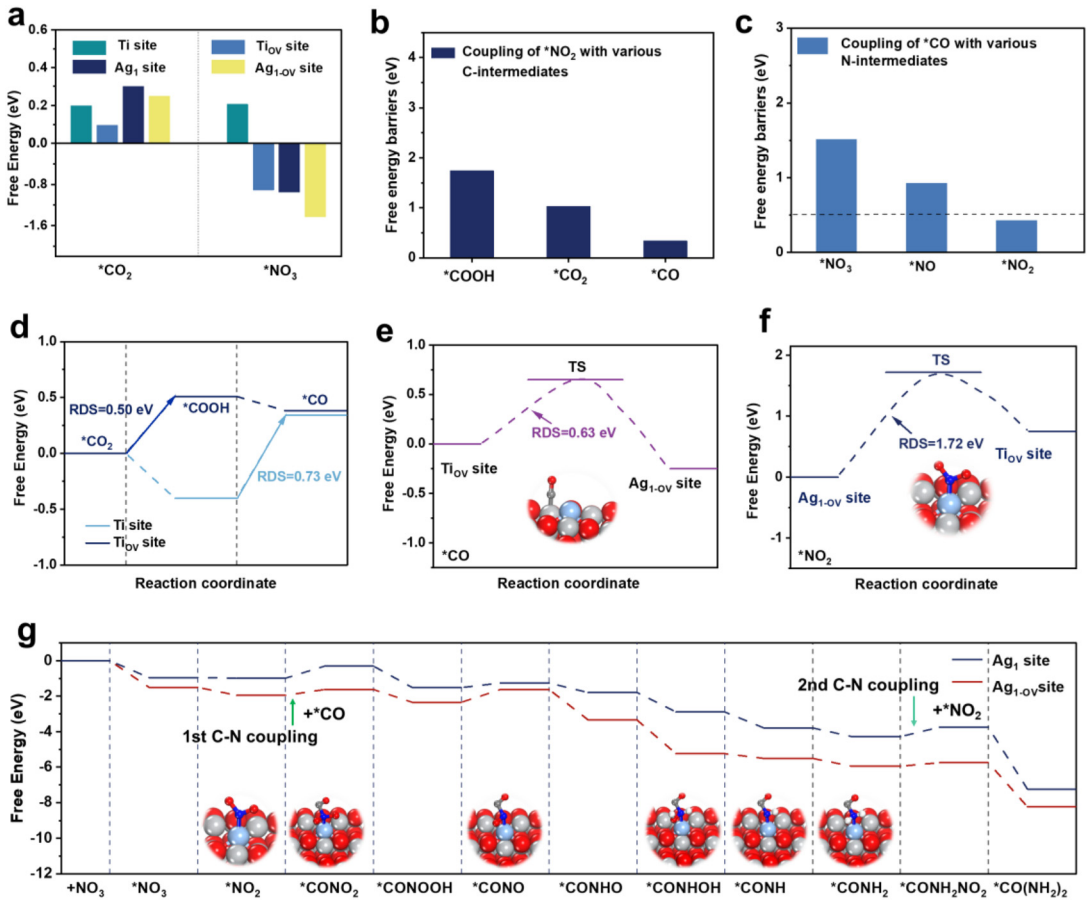

Fig. 4 (a) Adsorption free energies of $*CO_2$ and $*NO_2$ on various active sites (Ti site, Ag_1 site, Ti_{OV} site and $Ag_{1\text{-}OV}$ site) on Ag_1/TiO_{2-x}. (b and c) Free energy barriers of (b) coupling of $*NO_2$ with various C-intermediates and (c) coupling of *CO with various N-intermediates. (d) Free energy diagrams of $CO_2 \rightarrow *CO$ pathways. (e and f) Calculated TS energy barriers for the migration of (e) *CO from the Ti_{OV} site to the $Ag_{1\text{-}OV}$ site and (f) migration of $*NO_2$ from the $Ag_{1\text{-}OV}$ site to the Ti_{OV} site. (g) Free energy diagrams for the electrocatalytic C–N coupling of the $CO_2 + NO_3^-$ pathway on Ag_1/TiO_{2-x}.

the Ti_{OV} site drives $CO_2 \rightarrow *CO$ and the $Ag_{1\text{-}OV}$ site drives $NO_3^- \rightarrow *NO_2$. The migration of *CO from the Ti_{OV} site to the $Ag_{1\text{-}OV}$ site promotes selective C–N coupling with $*NO_2$ for urea formation.

In the UECN process, competing side reactions such as the NO_3RR and HER can impede selective urea synthesis. For the NO_3RR, as shown in Fig. S22, the free energy required for $*NO_2$ coupling with *CO to form $*CONO_2$ is significantly lower than that required for $*NO_2$ hydrogenation to NH_3, thereby favoring selective C–N coupling over NH_3 formation. Regarding the HER, the free energy calculations (Fig. S34) indicate that $Ag_{1\text{-}OV}$ and Ti_{OV} sites both preferentially bind NO_3^-/CO_2 over H. This selective NO_3^-/CO_2 adsorption over H is further supported by molecular dynamics (MD) simulations (Fig. S35), which show stronger catalyst–NO_3^- and catalyst–CO_2 interactions compared to the catalyst–H interaction.[40] These results demonstrate that Ag_1/TiO_{2-x} can well hamper the competitive NO_3RR and HER to result in high UECN selectivity for urea generation.

For $CO_2 + NO_3^-$ co-electrolysis in the UECN process, NO_3^- feedstock is known to be derived mainly from the Haber–Bosch-derived NH_3 that would compromise the sustainability and decarbonization objectives of electrocatalytic processes.[19] These challenges underscore the need for nitrogen sources that require facile activation with sustainable production. A breakthrough lies in plasma-assisted nitrogen oxidation, which converts atmospheric air (N_2/O_2) into nitrogen oxides (NO_x) *via* non-thermal plasma discharge.[41] Absorption of NO_x in alkaline solution generates NO_x^- ions (NO_2^-/NO_3^-).[41,42] Furthermore, plasma-derived NO_x^- leverages air as the sole nitrogen source, bypassing the fossil fuel-dependent NH_3 required for industrial urea synthesis and $CO_2 + NO_3^-$ co-electrolysis.[43] Accordingly, by integrating plasma-assisted air-to-NO_x^- conversion and $CO_2 + NO_x^-$ co-electrolysis (Fig. 5a), we propose a tandem plasma-electrochemical pathway that enables a truly sustainable urea synthesis, offering a viable pathway to mitigate global energy consumption and CO_2 emissions associated with the traditional industrial/electrochemical urea production.

For the initial plasma-assisted air oxidation, the plasma discharge across the needle electrode arrays generates a bright plasma zone (Fig. S36a) where high-energy electrons powerfully

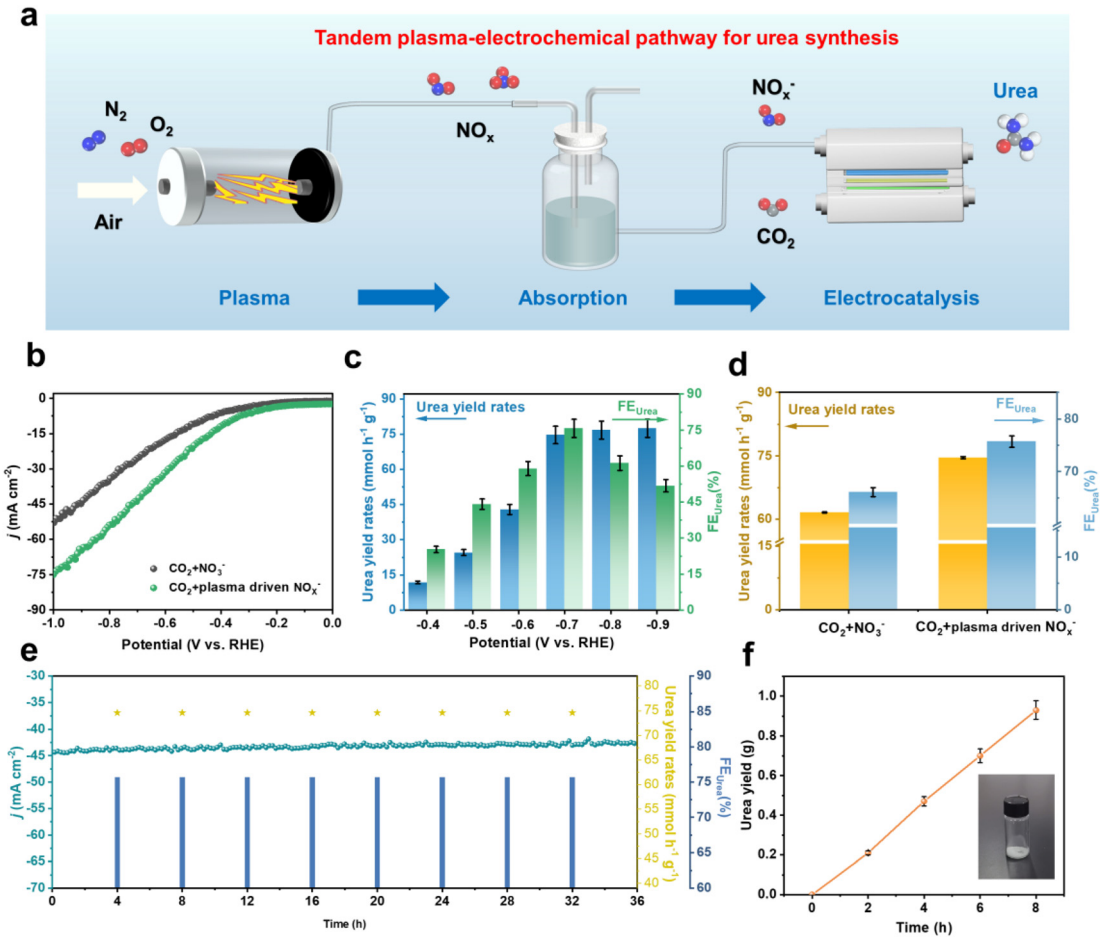

Fig. 5 (a) Schematic of the plasma-electrocatalytic process for urea synthesis from air and CO_2. (b) LSV curves of Ag_1/TiO_{2-x} in CO_2 + NO_3^- and CO_2 + NO_x^- electrolytes. (c) UECN performances of Ag_1/TiO_{2-x} at different potentials. (d) Comparison of urea yield rates and FE_{urea} after 1 h of electrolysis in different electrolytes at optimal potentials. (e) Long-term test of Ag_1/TiO_{2-x} at −0.7 V. (f) Urea yield over time.

activate N_2/O_2 molecules into reactive NO_x (NO/NO_2) gases, as evidenced by the gas stream transition from colorless to reddish-brown after 10 min of plasma discharge (Fig. S36b).[42] These generated NO_x gases are then absorbed into an alkaline KOH solution, resulting in the generation of NO_x^- (NO_2^-/NO_3^-) ions. Quantitative UV-vis analyses (Fig. S37 and S38) reveal that a prolonged plasma discharge time linearly enhances NO_x^- concentration, with NO_2^- as the dominant species (Fig. S39). After 60 min of continuous discharge, the total NO_x^- concentration reaches 118.8 mM, comprising 107.3 mM NO_2^- and 11.5 mM NO_3^- (Fig. S40, S41 and Table S3). Moreover, our plasma system presents remarkable stability, maintaining >100 mM NO_x^- yield across eight consecutive discharge cycles (Fig. S42), validating its robustness for stable production of NO_x^- feedstocks required for the downstream electrochemical co-reduction of CO_2 + NO_x^- to urea.

We then examined the UECN performance of Ag_1/TiO_{2-x} in a flow cell using a CO_2-saturated electrolyte containing plasma-derived NO_x^- (diluted to 0.1 M) and 0.1 M $KHCO_3$. As shown in Fig. 5b, the LSV curves present a marked enhancement in current density for CO_2 + NO_x^- (90.2% NO_2^-) co-electrolysis compared to CO_2 + NO_3^- co-electrolysis (Fig. 5b). Such a performance enhancement is attributed to the more efficient 12-electron transfer process of the CO_2 + NO_2^- pathway than the 16-electron pathway required for CO_2 + NO_3^- co-electrolysis. As shown in Fig. 5c, the Ag_1/TiO_{2-x} catalyst exhibits outstanding UECN performance, achieving an FE_{urea} of 75.7% and a urea yield of 74.6 mmol h^{-1} g^{-1} at −0.7 V, significantly superior to those obtained from CO_2 + NO_3^- co-electrolysis (Fig. 5d). Electrocatalytic stability tests indicate the stable current density and consistent performance of Ag_1/TiO_{2-x} over eight electrolysis cycles (Fig. 5e), highlighting the excellent catalytic stability. To produce high-purity urea on a large scale, the electrode area is expanded to 5 × 5 cm^2 with the catalyst loading increased to 20 mg. After 8 h of continuous electrolysis (Fig. 5f), 0.93 g of pure urea is obtained through electrolyte evaporation, sediment dissolution in benzene and benzene evaporation. This outcome highlights the technical viability of Ag_1/TiO_{2-x} catalysts for potential scalable urea production *via* a tandem plasma-electrocatalytic pathway.

In summary, Ag_1/TiO_{2-x} has been validated to be a highly efficient and durable UECN catalyst. Theoretical calculations

and *in situ* spectroscopic analyses unveil the synergistic roles of $Ag_{1\text{-}OV}$ and Ti_{OV} sites on Ag_1/TiO_{2-x} in promoting urea synthesis, where the Ti_{OV} site drives $CO_2 \rightarrow *CO$ and the $Ag_{1\text{-}OV}$ site drives $NO_3^- \rightarrow *NO_2$. The migration of *CO from a Ti_{OV} site to an $Ag_{1\text{-}OV}$ site promotes selective C–N coupling of *CO with $*NO_2$ for urea formation. Strikingly, by integrating plasma-assisted air-to-NO_x^- conversion and $CO_2 + NO_x^-$ co-electrolysis, Ag_1/TiO_{2-x} presents outstanding UECN performance with an FE_{urea} of 75.7% and a urea yield of 74.6 mmol h^{-1} g^{-1}. The present work opens up new avenues for effective and eco-friendly urea production, highlighting the transformative potential of coupled plasma-electrocatalysis technologies in advancing green chemical synthesis.

Conflicts of interest

The authors declare that they have no known competing financial interests or personal relationships that could have appeared to influence the work reported in this paper.

Data availability

The data supporting this article have been included as part of the supplementary information (SI). Supplementary information is available. See DOI: https://doi.org/10.1039/d5gc04601g.

Acknowledgements

This work was supported by the National Natural Science Foundation of China (52561042), the Gansu Province Joint Research Fund (24JRRA859) and the Industrial Support Plan Project of the Gansu Provincial Education Department (2024CYZC-22).

References

1 Y. Kohlhaas, Y. S. Tschauder, W. Plischka, U. Simon, R.-A. Eichel, M. Wessling and R. Keller, *Joule*, 2024, **8**, 1579–1600.
2 C. Mao, J. Byun, H. W. MacLeod, C. T. Maravelias and G. A. Ozin, *Joule*, 2024, **8**, 1224–1238.
3 X. Peng, L. Zeng, D. Wang, Z. Liu, Y. Li, Z. Li, B. Yang, L. Lei, L. Dai and Y. Hou, *Chem. Soc. Rev.*, 2023, **52**, 2193–2237.
4 Z. Lv, S. Zhou, L. Zhao, Z. Liu, J. Liu, W. Xu, L. Wang and J. Lai, *Adv. Energy Mater.*, 2023, **13**, 2300946.
5 Y. Yu, Z. Lv, Z. Liu, Y. Sun, Y. Wei, X. Ji, Y. Li, H. Li, L. Wang and J. Lai, *Angew. Chem., Int. Ed.*, 2024, **63**, e202402236.
6 Y. Yu, Y. Sun, J. Han, Y. Guan, H. Li, L. Wang and J. Lai, *Energy Environ. Sci.*, 2024, **17**, 5183–5190.
7 C. Lv, L. Zhong, H. Liu, Z. Fang, C. Yan, M. Chen, Y. Kong, C. Lee, D. Liu, S. Li, J. Liu, L. Song, G. Chen, Q. Yan and G. Yu, *Nat. Sustain.*, 2021, **4**, 868–876.
8 Y. Wan, M. Zheng, W. Yan, J. Zhang and R. Lv, *Adv. Energy Mater.*, 2024, **14**, 2303588.
9 J. Liu, Z. Li, C. Lv, X.-Y. Tan, C. Lee, X. J. Loh, M. H. Chua, Z. Li, H. Pan, J. Chen, Q. Zhu, J. Xu and Q. Yan, *Mater. Today*, 2024, **73**, 208–259.
10 R. Ge, J. Huo, P. Lu, Y. Dou, Z. Bai, W. Li, H. Liu, B. Fei and S. Dou, *Adv. Mater.*, 2024, **36**, 2412031.
11 F. Wang, J. Li, X. Xing, C. Yin, X. Wang, K. Chu and D. Ma, *Nano Lett.*, 2025, **25**, 13198–13205.
12 M. Xu, F. Wu, Y. Zhang, Y. Yao, G. Zhu, X. Li, L. Chen, G. Jia, X. Wu, Y. Huang, P. Gao and W. Ye, *Nat. Commun.*, 2023, **14**, 6994.
13 X. Wei, X. Wen, Y. Liu, C. Chen, C. Xie, D. Wang, M. Qiu, N. He, P. Zhou, W. Chen, J. Cheng, H. Lin, J. Jia, X.-Z. Fu and S. Wang, *J. Am. Chem. Soc.*, 2022, **144**, 11530–11535.
14 Y. Zhang, Z. Li, K. Chen, X. Yang, H. Zhang, X. Liu and K. Chu, *Adv. Energy Mater.*, 2024, **14**, 2402309.
15 X. Wei, C. Chen, X. Z. Fu and S. Wang, *Adv. Energy Mater.*, 2024, **14**, 2303027.
16 X. Wang, Q. Zhao, B. Yang, Z. Li, Z. Bo, K. H. Lam, N. M. Adli, L. Lei, Z. Wen and G. Wu, *J. Mater. Chem. A*, 2019, **7**, 25191–25202.
17 W. Zheng, C. Guo, J. Yang, F. He, B. Yang, Z. Li, L. Lei, J. Xiao, G. Wu and Y. Hou, *Carbon*, 2019, **150**, 52–59.
18 J. Chen, T. Wang, Z. Li, B. Yang, Q. Zhang, L. Lei, P. Feng and Y. Hou, *Nano Res.*, 2021, **14**, 3188–3207.
19 H. Xiong, P. Yu, K. Chen, S. Lu, Q. Hu, T. Cheng, B. Xu and Q. Lu, *Nat. Catal.*, 2024, **7**, 785–795.
20 W. Gou, H. Sun and F. Cheng, *Nano Res. Energy*, 2024, **3**, e9120121.
21 Y. Cheng, H. Wang, H. Song, K. Zhang, G. I. Waterhouse, J. Chang, Z. Tang and S. Lu, *Nano Res. Energy*, 2023, **2**, e9120082.
22 S. K. Kaiser, Z. Chen, D. Faust Akl, S. Mitchell and J. Pérez-Ramírez, *Chem. Rev.*, 2020, **120**, 11703–11809.
23 J. Zhai, T. Dong, Y. Zhou, J. Min, Y. Yan, C. S. Garoufalis, S. Baskoutas, D. Xu and Z. Zeng, *Nano Lett.*, 2023, **23**, 3239–3244.
24 J. Min, J. Zhai, T. Dong, D. Xu, Y. Yan, C. S. Garoufalis, S. Baskoutas, Z. Zeng and Y. Jia, *Nano Lett.*, 2023, **23**, 4648–4653.
25 Y. Zhang, S. Li, W. Zheng and X. Wang, *Nano Res. Energy*, 2023, **2**, e9120068.
26 K. Chen, D. Ma, Y. Zhang, F. Wang, X. Yang, X. Wang, H. Zhang, X. Liu, R. Bao and K. Chu, *Adv. Mater.*, 2024, **36**, 2402160.
27 W. Zheng, X. Yang, Z. Li, B. Yang, Q. Zhang, L. Lei and Y. Hou, *Angew. Chem., Int. Ed.*, 2023, **62**, e202307283.
28 J. Chen, X. Peng, Z. Li, B. Yang, Q. Zhang, J. Lu, L. Lei and Y. Hou, *Adv. Mater.*, 2025, **37**, 2409106.
29 L. Zeng, Z. Zhao, F. Lv, Z. Xia, S.-Y. Lu, J. Li, K. Sun, K. Wang, Y. Sun and Q. Huang, *Nat. Commun.*, 2022, **13**, 3822.

30 L. Li, G. Zhang, C. Zhou, F. Lv, Y. Tan, Y. Han, H. Luo, D. Wang, Y. Liu and C. Shang, *Nat. Commun.*, 2024, **15**, 4974.
31 S. Liu, J. Zhang, F. Li, J. P. Edwards, Y. C. Xiao, D. Kim, P. Papangelakis, J. Kim, D. Elder and P. De Luna, *Energy Environ. Sci.*, 2024, **17**, 1266–1278.
32 J. Shen and D. Wang, *Nano Res. Energy*, 2023, **3**, e9120096.
33 Z. Zhao, J. Zhang, M. Lei and Y. Lum, *Nano Res. Energy*, 2023, **2**, e9120044.
34 C. Lv, L. Zhong, H. Liu, Z. Fang, C. Yan, M. Chen, Y. Kong, C. Lee, D. Liu and S. Li, *Nat. Sustain.*, 2021, **4**, 868–876.
35 Y. Zhao, Y. Ding, W. Li, C. Liu, Y. Li, Z. Zhao, Y. Shan, F. Li, L. Sun and F. Li, *Nat. Commun.*, 2023, **14**, 4491.
36 Y. Gao, J. Wang, M. Sun, Y. Jing, L. Chen, Z. Liang, Y. Yang, C. Zhang, J. Yao and X. Wang, *Angew. Chem.*, 2024, **136**, e202402215.
37 J. Geng, S. Ji, M. Jin, C. Zhang, M. Xu, G. Wang, C. Liang and H. Zhang, *Angew. Chem., Int. Ed.*, 2023, **62**, e202210958.
38 T. Zhao, K. Chen, X. Xu, X. Li, X. Zhao, Q. Cai, K. Chu and J. Zhao, *Appl. Catal., B*, 2023, **339**, 123156.
39 D. Wu, K. Chen, P. Lv, Z. Ma, K. Chu and D. Ma, *Nano Lett.*, 2024, **24**, 8502–8509.
40 L. Xu, K. G. Papanikolaou, B. A. Lechner, L. Je, G. A. Somorjai, M. Salmeron and M. Mavrikakis, *Science*, 2023, **380**, 70–76.
41 L. Li, C. Tang, X. Cui, Y. Zheng, X. Wang, H. Xu, S. Zhang, T. Shao, K. Davey and S. Z. Qiao, *Angew. Chem., Int. Ed.*, 2021, **133**, 14250–14256.
42 X. Kong, J. Ni, Z. Song, Z. Yang, J. Zheng, Z. Xu, L. Qin, H. Li, Z. Geng and J. Zeng, *Nat. Sustain.*, 2024, **7**, 652–660.
43 J. Ding, W. Li, H. Zhang, S. Tang, Z. Mao, S. Zhang, M. Jin, Q. Lin, Y. Zhang and G. Wang, *Adv. Funct. Mater.*, 2024, **34**, 2410768.